

Article

Pyrogallol Detection Based on the Cobalt Metal–Organic Framework of Nanomaterial-Enhanced Chemiluminescence

Yanran Wang¹, Zhiqiang Wang¹, Yincheng Liu², Zixuan Liu², Zhan Gao², Kuangjun Li¹, Dajun Zhao³, Jing Wu^{1,*}  and Xuanhe Liu^{1,*}

¹ School of Science, China University of Geosciences (Beijing), Beijing 100083, China; yanran0406@163.com (Y.W.)

² School of Earth Sciences and Resources, China University of Geosciences (Beijing), Beijing 100083, China

³ School of Materials Science and Technology, China University of Geosciences (Beijing), Beijing 100083, China

* Correspondence: wujing@cugb.edu.cn (J.W.); liuxh@cugb.edu.cn (X.L.); Tel.: +86-10-8232-2758 (J.W.); Tel.: +86-10-8232-2758 (X.L.)

Abstract: The cobalt metal–organic framework (Co-MOF) is a kind of crystalline porous material within a periodic network structure, which is formed via the self-assembly of a Co metal center and a bridged organic ligand. In this paper, a Co-MOF was facilely synthesized via an ultrasonic method and applied to enhance the chemiluminescence (CL) emission of the NaIO₄-H₂O₂ system. The synthesized Co-MOF was nanosheet-like in nature and stacked in 2–3-micrometer flower shapes. Compared to the NaIO₄-H₂O₂ system without a Co-MOF, the CL intensity of the Co-MOF-NaIO₄-H₂O₂ system was enhanced about 70 times. This CL mechanism was determined to be a result of the synergistic effects of chemiluminescence resonance energy transfer (CRET) and electron–hole annihilation (EHA). The Co-MOF not only acted as a catalyst to accelerate the generation of reactive oxygen species in the CL reaction, but also worked as an emitter to further enhance the CL. Based on the Co-MOF-NaIO₄-H₂O₂ system, a highly sensitive CL analysis method was established for pyrogallol (PG) detection. Addition of PG into the CL system generated ¹O₂^{*}, which could transfer energy to the Co-MOF and further enhance the CL response. The enhanced CL was linear with the PG concentration. The CL analysis method exhibited a linear range of 1 × 10^{−4} M to 1 × 10^{−7} M, as well as having a linear correlation coefficient of 0.9995 and a limit of detection of (S/N = 3) of 34 nM.

Keywords: ultrasonic; Co-MOF; chemiluminescence; pyrogallol detection



check for updates

Citation: Wang, Y.; Wang, Z.; Liu, Y.; Liu, Z.; Gao, Z.; Li, K.; Zhao, D.; Wu, J.; Liu, X. Pyrogallol Detection Based on the Cobalt Metal–Organic Framework of

Nanomaterial-Enhanced

Chemiluminescence. *Chemosensors*

2023, 11, 395. [https://doi.org/](https://doi.org/10.3390/chemosensors11070395)

10.3390/chemosensors11070395

Academic Editor: Chung-Wei Kung

Received: 31 May 2023

Revised: 7 July 2023

Accepted: 8 July 2023

Published: 14 July 2023



Copyright: © 2023 by the authors. Licensee MDPI, Basel, Switzerland. This article is an open access article distributed under the terms and conditions of the Creative Commons Attribution (CC BY) license (<https://creativecommons.org/licenses/by/4.0/>).

1. Introduction

Pyrogallol (PG) belongs to the phenol family and is inherently toxic. However, as it is a chemical reagent and chemical raw material, PG is widely used in pharmaceutical synthesis, cosmetics, dyeing materials, and electronic products [1]. In the biomedical field, the interactions between PG analogs and biomacromolecules (e.g., protein, DNA/RNA, and polymers) can be used for the design of useful biomedical materials [2]. Due to the widespread use of PG, it is consequentially discharged into industrial effluents and, thus, adds hazards into aquatic environments. PG can cause oxidative stress, which may lead to biological poisoning or even death [3–5]. The abundance of PG in rivers is about 4 μM [6]. For As4.1 juxtaglomerular cells, the IC₅₀ of PG is about 60 μM for 48 h, as determined using an MTT assay [7]. Many analytical methods have been designed for PG detection [8–12], but they show the disadvantages of high-cost, complicated and time-consuming procedures, and low sensitivity. Therefore, it is necessary to establish a new cost-effective technique for PG detection that is characterized by high sensitivity, ease of operation, and rapid analysis.

Chemiluminescence (CL) analysis is a characteristic method used in analytical chemistry, as well as in environmental monitoring, drug analysis, food testing, biological analysis, and clinical detection, because of its simple equipment, convenient operation, rapid analysis, and easy automation [13–17]. However, it is undeniable that the CL analysis

method still has limitations, such as easy interference, poor selectivity, and low signal response [18,19]. Selecting appropriate sensitizers and adding them into CL systems is an effective route toward enhancing CL intensity and improving both sensitivity and accuracy. The development of nanomaterials sheds light on ways to devise novel CL sensitizers [20]. Nanomaterials can enhance CL intensity in two ways: chemiluminescence resonance energy transfer (CRET) and electron–hole annihilation (EHA). CRET is a process through which energy transfers from a CL reagent to an energy acceptor during the CL reaction; EHA is a process through which the nanomaterials serve as CL emitters in order to produce enhanced CL from the combination of hole- and electron-injected nanomaterials [19,21]. Metal–organic frameworks (MOFs) represent a new class of nanomaterials, and they are composed of metal nodes and organic ligands and have become one of the most attractive materials due to their tunable structure and function [22,23]. Due to their porous structure and low energy band, many researchers have begun to pay attention to their application. For example, Singh et al. [24] prepared a two-fold, interpenetrated, and mixed-ligand Cd(II)-organic framework with great photoluminescence (PL) with which to detect Fe³⁺ and Cr (IV). Liu et al. [25] designed a Zn-MOF with a new organic linker, which contained a pyridine group, was able to absorb CO₂ due to its large specific surface area and porous structure, and could also detect Cu²⁺ due to its excellent PL properties. Therefore, it is an appealing research direction regarding the application of MOF materials with specific energy levels and porous molecular structures to sensitize the CL process [26]. However, MOFs used in aqueous solutions have poor stability and dispersity, meaning that their applications in liquid-phase CL systems face serious challenges. Additionally, MOFs are always synthesized through hydro- and solvo-thermal reactions, which involve energy- and time-consuming steps and impede their CL applications [27]. Therefore, novel MOFs with higher stability and better dispersity need to be designed and synthesized through facile and economical approaches in order to enhance CL intensity for sensitive detection.

In this work, we synthesized a cobalt metal–organic framework (Co-MOF) using an ultrasonic method that used 2-aminoterephthalic acid (NH₂-H₂BDC) as a ligand and applied it to sensitize the ultraweak CL system of NaIO₄-H₂O₂. The Co-MOF dramatically enhanced the CL response of the NaIO₄-H₂O₂ system. Optimum CL signals were obtained by optimizing experimental conditions. The CL process was systematically studied and demonstrated to occur via two synergistic mechanisms: CRET and EHA. The CL signals showed a linear relationship with the concentration of PG within a specific range. As a result, the Co MOF-NaIO₄-H₂O₂ system was developed as a CL analysis method for PG detection, having the advantages of high sensitivity, good reproducibility, and fast analysis speed.

2. Materials and Methods

2.1. Reagents and Materials

Sulfuric acid (H₂SO₄, 98%) was purchased from Beijing Chemical Reagent Co. (Beijing, China). Hydrogen peroxide (H₂O₂, 30%), ethanol (99.7%) and isopropyl alcohol (98.5%) were supplied by Sinopharm Chemical Reagent Co., Ltd. (Shanghai, China). Cobalt chloride hexahydrate (CoCl₂·6H₂O, 99%), *N,N*-dimethylformamide (DMF, C₃H₇NO, 99.9%), triethylamine (C₆H₁₅N, 99.5%), NH₂-H₂BDC (C₈H₇NO₄, ≥98%) and PG (C₆H₆O₃, 99%) were obtained from Beijing InnoChem Science and Technology Co., Ltd. (Beijing, China). Sodium periodate (NaIO₄, ≥99.5%), *p*-benzoquinone (BQ, C₆H₄O₂, 99.7%) and thiourea (99%) were purchased from Aladdin Reagent Co., Ltd. (Shanghai, China). Ascorbic acid (AA, C₆H₈O₆, ≥99%), 5,5-dimethyl-1-pyrroline-N-oxide (DMPO, C₆H₁₁NO) and 2,2,6,6-tetramethylpiperidine (TEMP, C₉H₁₉N) were bought from Sigma-Aldrich Chemical Co. (St. Louis, MO, USA). In a typical experiment, none of the chemicals were further purified.

2.2. Apparatus

The scanning electron microscope (SEM) images were obtained via a JSM-7900 scanning electron microscope (JEOL, Tokyo, Japan) to study the micro-morphologies of the

samples. The transmission electron microscopy (TEM) image and selected area electron diffraction (SAED) patterns were determined via a JEOL-1400 transmission electron microscope (JEOL, Tokyo, Japan). Energy-dispersive X-ray spectroscopy (EDS) was recorded on a JED-2300 T transmission electron microscope (JEOL, Tokyo, Japan). The elemental composition of the surface of the material was measured via the X-ray photoelectron spectrometry (XPS) tool created by AXIS SUPRA, Shimadzu, Kyoto, Japan. Fourier transform infrared (FT-IR) spectra were used to determine functional groups and structures depending on PerkinElmer Frontier FT-IR spectrometer. The PL spectra were determined via an Agilent Cary Eclipse spectrofluorometer (F-7000, Hitachi, Japan) with a 5-nanometer slit width. UV-vis absorption spectra were collected via a PerkinElmer Lambda 950 spectrophotometer. The batch experiment was performed via a BPCL ultraweak CL analyzer (BPCL-GP21Q-TGC, Guangzhou microlight technology Co., Ltd., Guangzhou, China), and the voltage of the photomultiplier tube (PMT) was controlled at 700 V. CL spectra were collected via an FLS-1000 steady-state/transient fluorescence spectrometer (Edinburgh Instruments Ltd., Livingstone, Edinburgh, UK). Electron paramagnetic resonance (EPR) spectra were determined via a Bruker E500 spectrometer to make sure that the correct free radicals were generated. Brunauer–Emmett–Teller (BET) surface areas and pore size distribution were detected via the autosorb iQ analyzer (Quantachrome Instruments Co., Ltd., Boynton Beach, FL, USA).

2.3. Synthesis of Co-MOF

Co-MOF was synthesized via the ultrasonic method illustrated in previous literature [28]. Firstly, 32 mL DMF, 2 mL C₂H₅OH and 2 mL H₂O were mixed in a 100-milliliter flask. Subsequently, 0.75 mmol of NH₂-H₂BDC was added into the above flask and dissolved using an ultrasonic wave. Next, 0.75 mmol of CoCl₂·6H₂O was added and ultrasonically treated until completely dissolved. Finally, 0.8 mL of triethylamine was quickly poured into the flask and vigorously stirred for 5 min. The flask was kept under ultrasonic treatment for 8 h at a power of 90 kHz under ambient conditions. The resulting product was then centrifuged at a speed of 10,000 rpm for 5 min to remove the supernatant, washed twice with C₂H₅OH and dispersed in 30 mL of H₂O. The washed product was freeze-dried under a vacuum and then collected for further use. The ultrasonic time for Co-MOF synthesis was further optimized to obtain the best CL enhancement.

2.4. CL Emission Study of the Co-MOF-NaIO₄-H₂O₂ System

All of the CL signals were collected via the BPCL luminescence analyzer at a time interval of 0.01 s. The PMT was operated at a voltage of 1000 V. In total, 1 mL of 0.08 M NaIO₄ solution and 100 μL of 4 mg·mL⁻¹ Co-MOF were mixed into the CL reaction cell. Next, 1 mL of 0.12 M H₂O₂ solution (acidified by 0.006 M H₂SO₄) was rapidly injected, and the CL reaction was triggered. The CL intensity was measured, and the kinetic curves were collected. A control experiment was conducted without Co-MOF to demonstrate the effect of Co-MOF on the CL process of NaIO₄-H₂O₂ system. In order to obtain the optimum CL emission, the concentrations of all of the substances in the CL system were optimized using the univariate method. The CL intensities were measured at a series of concentrations of Co-MOF (1 mg·mL⁻¹, 2 mg·mL⁻¹, 3 mg·mL⁻¹, 4 mg·mL⁻¹, 5 mg·mL⁻¹, and 6 mg·mL⁻¹) and H₂O₂ (0.04 M, 0.08 M, 0.10 M, 0.12 M, 0.14 M and 0.16 M), NaIO₄ (0.01 M, 0.02 M, 0.03 M, 0.04 M, 0.05 M, 0.06 M, 0.07 M, 0.08 M, 0.09 M, and 0.10 M), as well as different concentration of H₂SO₄ (0.002 M, 0.003 M, 0.004 M, 0.005 M, 0.006 M, 0.007 M, 0.008 M, and 0.009 M) to adjust pH values. The following experiments were carried out under optimal conditions.

2.5. CL Mechanism Study of the Co-MOF-NaIO₄-H₂O₂ System

EPR and free radical quenching experiments were the two main methods used to explore the CL mechanism of the Co-MOF-NaIO₄-H₂O₂ system. The EPR spectrum was collected at the X-band frequency of 9.85 GHz using a 300 W xenon lamp

(300 nm < λ < 1100 nm) as the light source. The output radiation was focused on the sample in the cavity through an optical fiber (50 cm in length, 0.3 cm in diameter). TEMP and DMPO were used as the specific detection reagents for $^1\text{O}_2$, $\cdot\text{OH}$, and $\cdot\text{O}_2^-$. In the free-radical-quenching experiments, specific free-radical quenchers were used to detect the free-radical intermediates of the reaction system. Furthermore, the role of dissolved oxygen in the system was analyzed through the bubbling experiment of oxygen and nitrogen. CL kinetic curves were collected, with all of the solutions pre-treated with nitrogen. In the control experiment, the solutions were first treated with nitrogen and then treated with oxygen. Moreover, CL kinetic curves were collected via various injection sequences of reagents. Three different injection sequences were investigated. The first way was to add acidified H_2O_2 into the mixture of NaIO_4 and Co-MOF, the second way was to inject NaIO_4 into the mixture of Co-MOF and acidified H_2O_2 , and the third way was to infuse Co-MOF into the mixed solution of NaIO_4 and acidified H_2O_2 . CL spectrum and UV-Vis spectrum tests were also conducted to verify the CL mechanism.

2.6. PG Detection

The constructed Co-MOF- NaIO_4 - H_2O_2 system was developed as a CL sensor for PG detection. Calibration curve was recorded by detecting the relationship between CL intensities and PG concentration series under the optimal experimental conditions. Next, 100 μL PG (dissolved in H_2O), 1 mL 0.08 M NaIO_4 solution, and 100 μL 4 $\text{mg}\cdot\text{mL}^{-1}$ Co-MOF were mixed into the CL reaction cell. Finally, 1 mL of 0.12 M H_2O_2 solution (acidified by 0.006 M H_2SO_4) was injected to detect the CL signals.

3. Results and Discussion

3.1. Characterization of Co-MOF

The ultrasonic synthesized Co-MOF displayed a flower-shaped morphology with a diameter of approximately 2~3 μm (Figure 1a). This morphology was formed by stacking several pieces of nanosheets, which were transparent and ultrathin (Figure 1b). The large surface and numerous active sites of Co-MOF nanosheets were conducive to the CL reactions. The SAED image in Figure 1b's inset image demonstrates the single-crystal diffraction properties of the Co-MOF. The XRD pattern confirmed the high crystallinity of Co-MOF and coincided with the simulated pattern of cobalt-based ultrathin MOFs nanosheets (Figure 1h) [28,29]. The EDS-mapping diagram showed the composition of the Co-MOF, which was composed of Co, C, N, and O uniformly distributed across the nanosheets (Figure 1c). XPS was utilized to corroborate the chemical composition and provide further information on the surface electronic state of the Co-MOF (Figure 1d). As shown in Figure 1e, the characteristic signals at 781.6 eV and 797.6 eV were attributed to Co 2p_{3/2} and Co 2p_{1/2}, respectively [30]. Satellite peaks accompanying them at 786.4 eV and 802.7 eV revealed the formation of antibonding orbitals between the Co and O elements [31]. The characteristic signal of O 1s at 531.8 eV and its fitting peaks at 531.6 eV, 532.1 eV, and 533.4 eV were attributed to Co-O, C-O, and C=O, respectively (Figure 1f) [29]. The signature signal of C is located at 283.6 eV and 287.4 eV, and its fitting peaks located at 283.4 eV, 284.8 eV, and 287.4 eV were attributed to C-C, C-O-C, and O-C=O, respectively (Figure 1g) [28]. All of the above results confirmed the successful coordination between Co^{2+} and $\text{NH}_2\cdot\text{H}_2\text{BDC}$. The coordination between Co^{2+} and $\text{NH}_2\cdot\text{H}_2\text{BDC}$ was further verified via the FT-IR spectra (Figure 1i). Apparent differences were observed via the FT-IR spectra of Co-MOF and $\text{NH}_2\cdot\text{H}_2\text{BDC}$. The -OH in the -COOH group of $\text{NH}_2\cdot\text{H}_2\text{BDC}$ had a broad-stretching vibrational absorption peak in the region of 3000 cm^{-1} to 2500 cm^{-1} . In contrast, the peak of Co-MOF disappeared within the FT-IR spectra due to the deprotonation of $\text{NH}_2\cdot\text{H}_2\text{BDC}$ during the coordination process [29]. Compared to the FT-IR spectra of $\text{NH}_2\cdot\text{H}_2\text{BDC}$, three new peaks appeared at the low wavenumbers of 708 cm^{-1} , 450 cm^{-1} , and 423 cm^{-1} , which were attributed to the stretching vibration of Co-O [29,32,33]. In addition, the stretching vibration peak of the H_2O molecule at 3087 cm^{-1} indicated that Co^{2+} also coordinated with H_2O in Co-MOF. Asymmetric and symmetric stretching vibration

absorptions in the $-\text{COO}-$ group in the ligand $\text{NH}_2\cdot\text{H}_2\text{BDC}$ resulted in the two peaks located at 1558 cm^{-1} and 1381 cm^{-1} , respectively. The peaks at 3473 cm^{-1} and 3342 cm^{-1} were derived from the asymmetric and symmetric stretching vibrations in the $-\text{NH}_2$ group in the ligand $\text{NH}_2\cdot\text{H}_2\text{BDC}$. The intensities of the two peaks in the FT-IR spectra of Co-MOF were significantly weaker than those of the FT-IR spectra of $\text{NH}_2\cdot\text{H}_2\text{BDC}$, further indicating the coordination effect of $\text{NH}_2\cdot\text{H}_2\text{BDC}$ [29,33,34]. As shown in Figure 1j's inset image, the prepared Co-MOF exhibited a bright blue color under the UV lamp ($\lambda_{\text{ex}} = 365\text{ nm}$). Co-MOF gave an emission centered at 420-nanometer excitation due to lights with different wavelengths varying from 320 nm to 400 nm (Figure 1j).

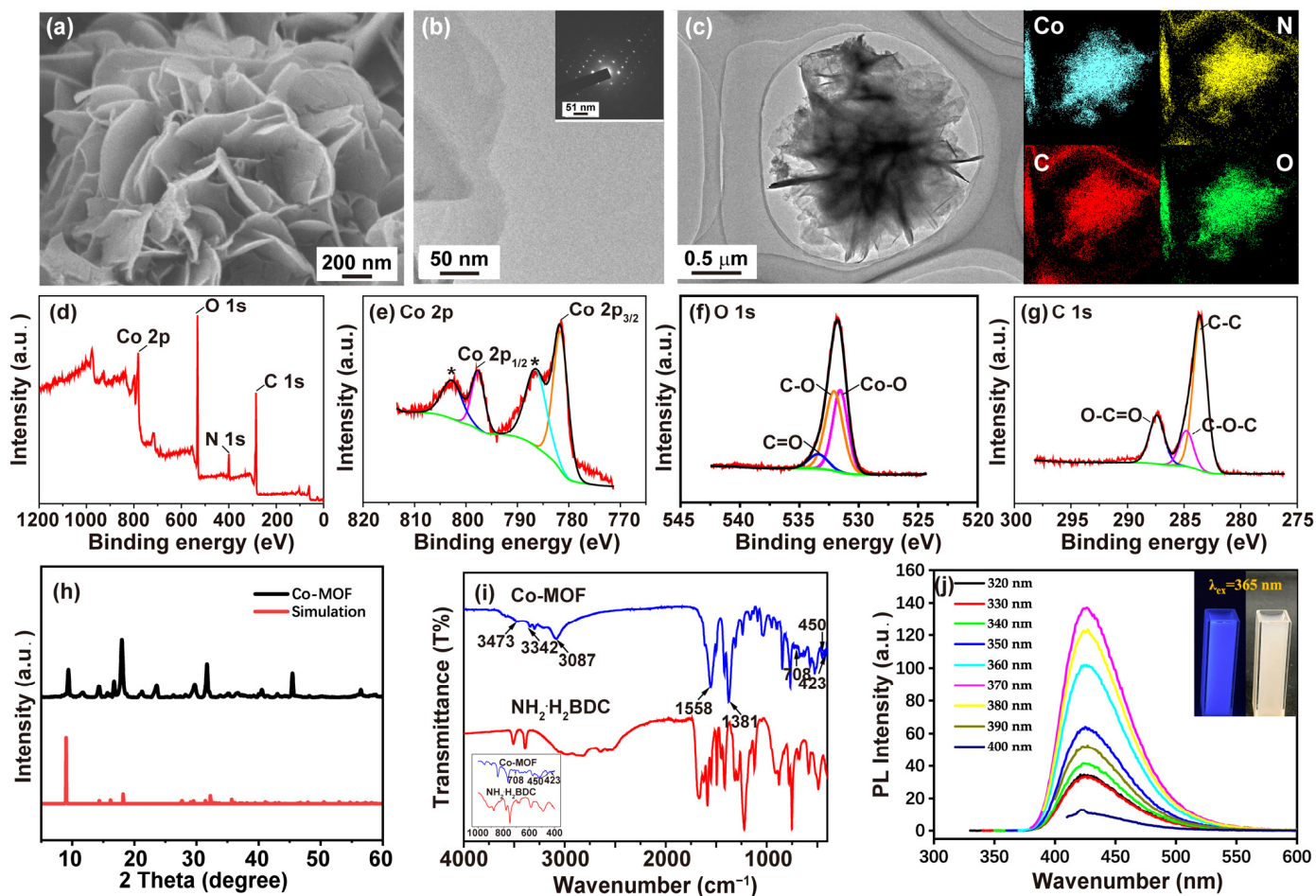


Figure 1. Characterization of ultrasonically synthesized Co-MOF: (a) SEM image of Co-MOF; (b) TEM image of Co-MOF, and the inset image is the SAED image of Co-MOF; (c) EDS-mapping analysis of Co-MOF, (blue refers to cobalt element, yellow refers to nitrogen element, red refers to carbon element, and green refers to oxygen element); (d) XPS survey of Co-MOF; (e) high-resolution XPS spectra of Co 2p of Co-MOF (peaks marked with * revealed the formation of antibonding orbitals between the Co and O elements); (f) High-resolution XPS spectra of O 1s of Co-MOF; (g) high-resolution XPS spectra of C 1s of Co-MOF; (h) XRD pattern of the as-synthesized Co-MOF (black) and simulated XRD pattern of cobalt-based ultrathin MOFs nanosheets (red); (i) FT-IR spectra of Co-MOF and $\text{NH}_2\cdot\text{H}_2\text{BDC}$; (j) PL spectra of Co-MOF, and the inset image is the photograph of Co-MOF under a UV lamp ($\lambda_{\text{ex}} = 365\text{ nm}$).

The hydrothermal synthesized Co-MOF displayed a morphology completely different to that of the ultrasonic synthesized Co-MOF. As shown in Figure 2a,b, the Co-MOF synthesized via the hydrothermal method exhibited a regular circular shape, rather than

layer stacked flower shape, and its size was approximately 500 nm and 1 μm , which was slightly smaller than the size of Co-MOF synthesized via ultrasound.

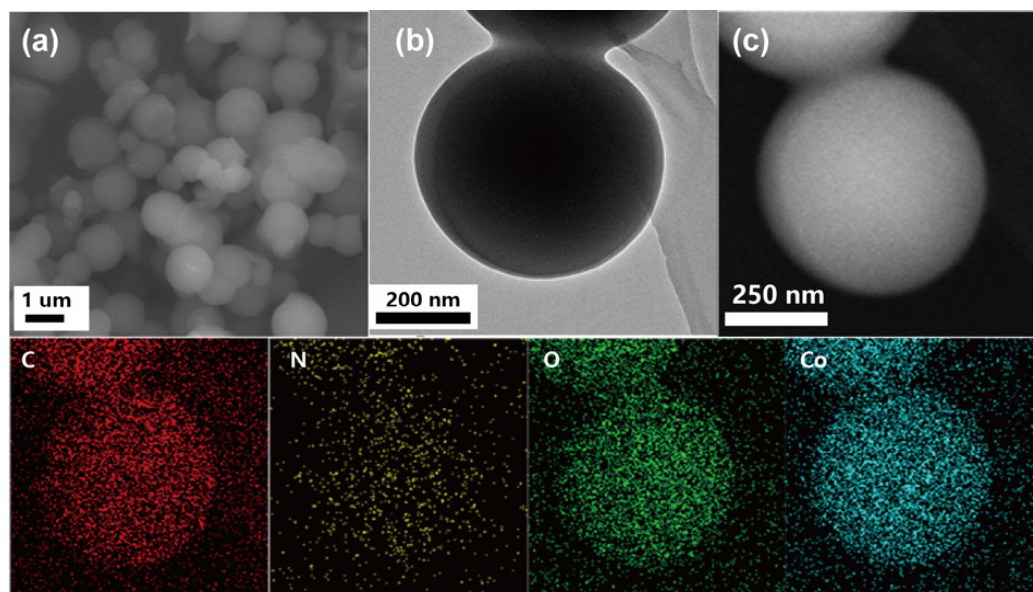


Figure 2. Characterization of hydrothermally synthesized Co-MOF: (a) SEM image of Co-MOF; (b) TEM image of Co-MOF; (c) EDS-mapping analysis of Co-MOF (red color refers to carbon element, yellow color refers to nitrogen element, green color refers to oxygen element, and blue color refers to cobalt element).

3.2. CL Emission of the Co-MOF- $\text{NaIO}_4\text{-H}_2\text{O}_2$ System

As shown in Figure 3a, the ultraweak CL emission of the $\text{NaIO}_4\text{-H}_2\text{O}_2$ system was dramatically enhanced using the ultrasonic synthesized Co-MOF. Free Co^{2+} ions were also tested by adding CoCl_2 solution into the $\text{NaIO}_4\text{-H}_2\text{O}_2$ system, while its CL enhancement was negligible, indicating that the CL enhancement was rooted from Co-MOF. In comparison, the CL enhancement of hydrothermally synthesized Co-MOF was also tested and demonstrated to be weaker than that of ultrasonically synthesized Co-MOF (Figure 3b). Ultrasonic waves proved able to have a certain effect on the synthesized Co-MOF and the CL emission performed via the Co-MOF- $\text{NaIO}_4\text{-H}_2\text{O}_2$ system. The N_2 adsorption and desorption isotherms were carried out to examine the differences between the specific surface areas and pore sizes of the hydrothermally synthesized and ultrasonically synthesized Co-MOFs to explore the effect of ultrasonic waves (Figure 4). All of the isotherms (red line in Figure 4) displayed a closed hysteresis loop of type H3, demonstrating that a type IV classification (BDDT classification) was available for them, and the samples exhibited mesoporous structures. According to the multi-point BET calculations, the specific surface area of the Co-MOF synthesized via the ultrasonication method was $27.42 \text{ m}^2/\text{g}$, while that of the Co-MOF synthesized via the hydrothermal method was $10.88 \text{ m}^2/\text{g}$. As shown in the inset of Figure 4a and b, the main pore sizes of ultrasonically synthesized and hydrothermally synthesized Co-MOF were identified via the Barrett–Joyner–Halenda (BJH) model to be 29.83 and 3.80 nm, respectively. Larger pores in ultrasonically synthesized Co-MOF demonstrated more structural defects that were caused by ultrasonic waves. The larger specific surface areas and greater structural defects of the ultrasonically synthesized Co-MOF was promising for CL enhancement.

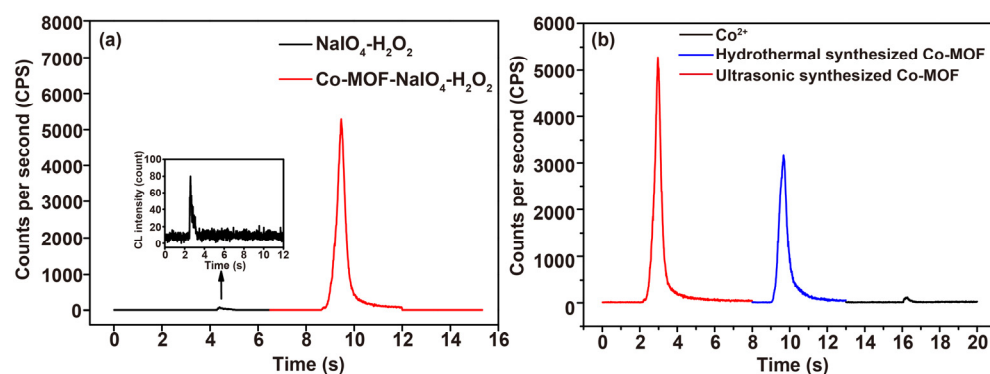


Figure 3. CL enhancement of Co-MOF: (a) the comparison between CL intensities of $\text{NaIO}_4\text{-H}_2\text{O}_2$ system and the $\text{Co-MOF-NaIO}_4\text{-H}_2\text{O}_2$ system (conditions: $4 \text{ mg}\cdot\text{mL}^{-1}$ Co-MOF, $0.12 \text{ M H}_2\text{O}_2$ acidified using $0.006 \text{ M H}_2\text{SO}_4$ and 0.08 M NaIO_4); (b) the comparison between CL intensities of $\text{CoCl}_2\text{-NaIO}_4\text{-the H}_2\text{O}_2$, Co-MOF (hydrothermal synthesized)- $\text{NaIO}_4\text{-H}_2\text{O}_2$, and Co-MOF (ultrasonic synthesized)- $\text{NaIO}_4\text{-H}_2\text{O}_2$ systems (conditions: $4 \text{ mg}\cdot\text{mL}^{-1}$ CoCl_2 , $4 \text{ mg}\cdot\text{mL}^{-1}$ Co-MOF, $0.12 \text{ M H}_2\text{O}_2$ acidified using $0.006 \text{ M H}_2\text{SO}_4$ and 0.08 M NaIO_4).

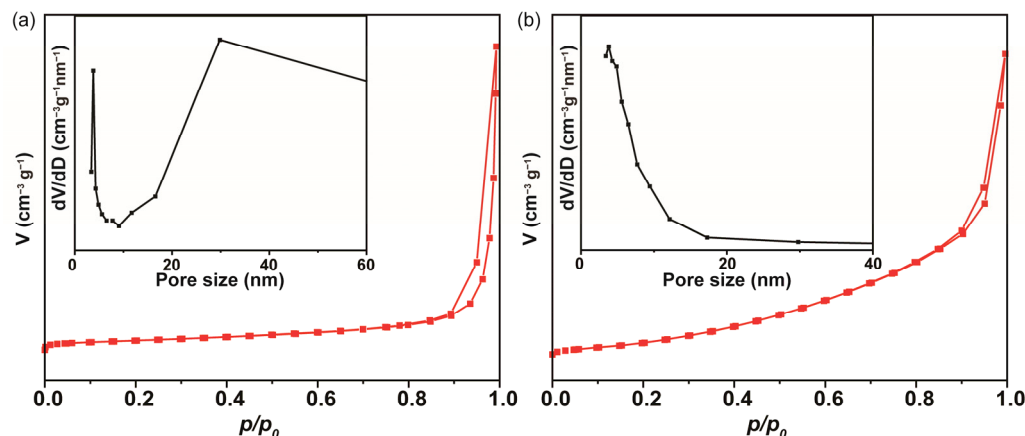


Figure 4. The N_2 adsorption and desorption isotherms of the Co-MOF synthesized via different methods: (a) sonication method; (b) hydrothermal method. The insets are the pore sizes of the Co-MOF synthesized via the sonication and hydrothermal methods.

Subject to the optimal CL response, the experimental parameters of the $\text{Co-MOF-NaIO}_4\text{-H}_2\text{O}_2$ system were systematically optimized via the univariate method. The effects of the ultrasonic time required for Co-MOF synthesis and the concentrations of Co-MOF, H_2SO_4 (to adjust the optimal pH), H_2O_2 , and NaIO_4 on the CL intensity were separately investigated. The effect of the Co-MOF synthesis time on the CL of the $\text{Co-MOF-NaIO}_4\text{-H}_2\text{O}_2$ system is shown in Figure 5a. The Co-MOF had the best enhancement effect on the CL intensity of $\text{NaIO}_4\text{-H}_2\text{O}_2$ system after 8 h of ultrasonic synthesis. The CL intensity of the $\text{Co-MOF-NaIO}_4\text{-H}_2\text{O}_2$ system increased with the increase in Co-MOF amount until it reached $4 \text{ mg}\cdot\text{mL}^{-1}$ (Figure 5b). According to preliminary experiments, the $\text{Co-MOF-NaIO}_4\text{-H}_2\text{O}_2$ system has excellent CL performance under H_2SO_4 acidification conditions. When $0.12 \text{ M H}_2\text{O}_2$ was acidified with $0.006 \text{ M H}_2\text{SO}_4$, the CL intensity of the system was highest (Figure 5c,d). The CL signal of the system was optimal when the concentration of NaIO_4 was 0.08 M (Figure 5e). Unless otherwise specified, subsequent experiments were carried out under optimal experimental conditions.

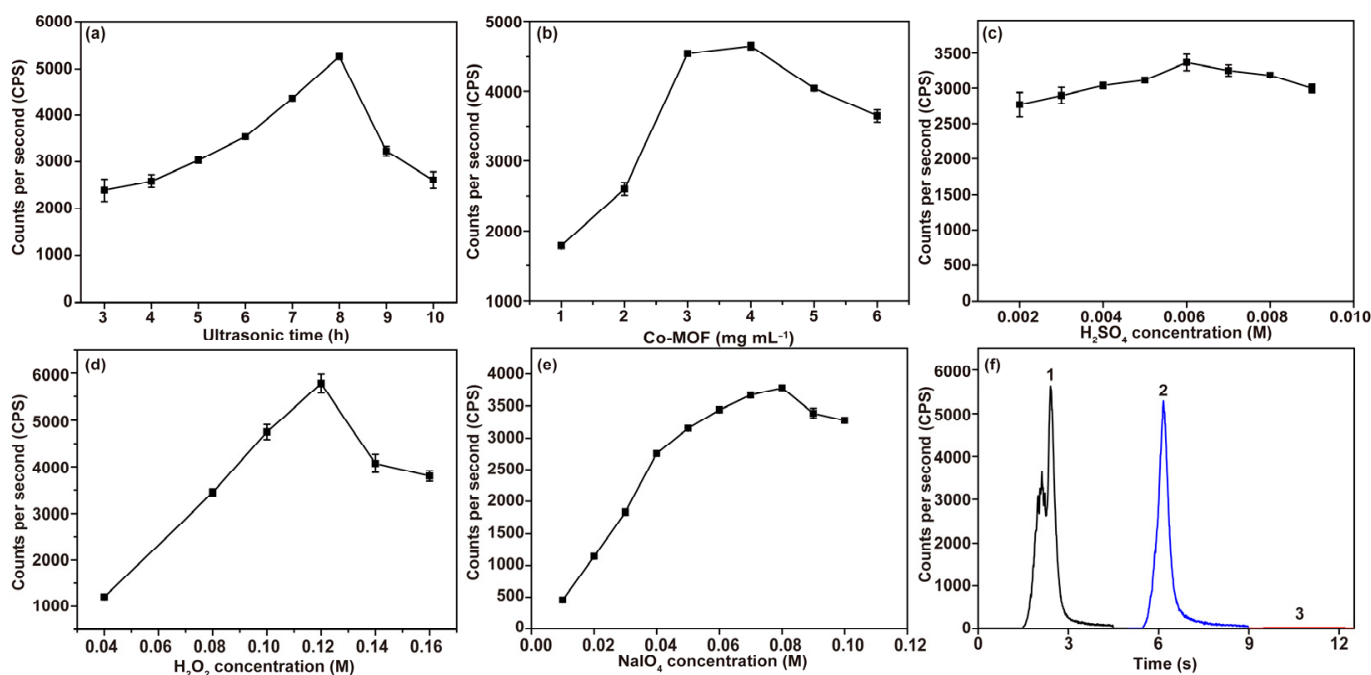


Figure 5. Optimization of experimental conditions in the Co-MOF–NaIO₄–H₂O₂ system. (a) Ultrasonic time required for Co-MOF synthesis was optimized (conditions: 4 mg·mL⁻¹ Co-MOF, 0.12 M H₂O₂ acidified using 0.006 M H₂SO₄ and 0.08 M NaIO₄); (b) the amount of Co-MOF added into the NaIO₄–H₂O₂ system was optimized (conditions: 0.12 M H₂O₂ acidified using 0.006 M H₂SO₄ and 0.08 M NaIO₄); (c) H₂SO₄ concentration was optimized (conditions: 4 mg·mL⁻¹ Co-MOF, 0.12 M H₂O₂ and 0.08 M NaIO₄); (d) NaIO₄ concentration was optimized (conditions: 4 mg·mL⁻¹ Co-MOF and 0.12 M H₂O₂ acidified using 0.006 M H₂SO₄); (e) H₂O₂ concentration was optimized (conditions: 4 mg·mL⁻¹ Co-MOF, 0.006 M H₂SO₄ and 0.08 M NaIO₄); (f) optimization of the reagent mixing order of the Co-MOF–NaIO₄–H₂O₂ system (conditions: 4 mg·mL⁻¹ Co-MOF, 0.12 M H₂O₂ acidified using 0.006 M H₂SO₄ and 0.08 M NaIO₄). Legend: (1) injection of NaIO₄ into the mixture of Co-MOF and H₂O₂; (2) injection of H₂O₂ into the mixture of Co-MOF and NaIO₄; (3) injection of Co-MOF into the mixture of NaIO₄ and H₂O₂.

Moreover, different injection sequences of reagents in the system are essential factors that affect CL intensity. Therefore, the influence of these sequences on the CL intensity of the system needs to be investigated. Under the optimal experimental conditions, the most robust CL kinetic curves were obtained when NaIO₄ solution was injected into the mixture of acidic H₂O₂ and Co-MOF (Figure 5f). The reason for this outcome is that Co-MOF acts as a catalyst that accelerates the reaction of H₂O₂ decomposition to generate ·OH, which is beneficial for CL process. However, since the system underwent two CL reactions, the CL kinetic curve showed a shoulder peak that was not favorable for detection. The subsequent experiments were conducted by injecting acidic H₂O₂ solution into the mixture containing NaIO₄ and Co-MOF.

3.3. CL Mechanism of the Co-MOF–NaIO₄–H₂O₂ System

Nanomaterials introduced into liquid-phase CL systems generally act as catalysts [35] and luminophores [36,37]. To elucidate the role of Co-MOF and the main light emission species of the system, the CL spectra of the Co-MOF–NaIO₄–H₂O₂ system were collected using a transient fluorescence spectrometer. The results showed that the system had a maximum CL emission of 470 nm and the luminescence range was 350–600 nm (Figure 6a), which overlapped with the emission band of dimol singlet oxygen ¹(O₂)₂ [38–40] and Co-MOF. Therefore, (¹O₂)₂* and Co-MOF* were speculated to be the main emitters present in the Co-MOF–NaIO₄–H₂O₂ system. Figure 6b shows the UV-Vis spectra in which the

NaIO_4 , H_2O_2 , $\text{NaIO}_4\text{-H}_2\text{O}_2$, Co-MOF-NaIO_4 , and $\text{Co-MOF-NaIO}_4\text{-H}_2\text{O}_2$ systems had no characteristic absorption peaks. In contrast, Co-MOF had a prominent strong characteristic absorption peak at 300–400 nm. After the addition of H_2O_2 , the absorption peak decreased, and its position was redshifted, demonstrating that Co-MOF catalyzed H_2O_2 to give $\cdot\text{OH}$ and reacted with $\cdot\text{OH}$. As a result, H_2O_2 , which is a strong oxidant, also produced a weak and rapidly quenched CL signal when mixed with Co-MOF (Figure 6c, black line). The disappeared absorption peak of Co-MOF at 300–400 nm in the Co-MOF-NaIO_4 system further proved that Co-MOF not only played the role of catalyst in this system, but also participated in the reaction [41]. This phenomenon was certified based on the weak CL signals noted in Figure 6c (blue line). In addition, no other absorption peaks were observed; thus, it was clear that substances with additional UV-vis absorption were not produced via the CL system.

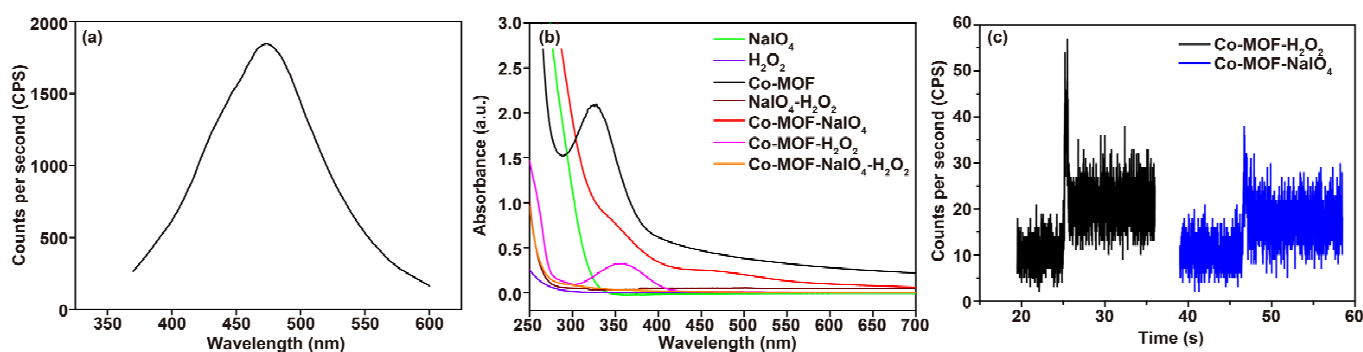


Figure 6. A study on the CL mechanism of the $\text{Co-MOF-NaIO}_4\text{-H}_2\text{O}_2$ system: (a) CL spectra of the $\text{Co-MOF-NaIO}_4\text{-H}_2\text{O}_2$ system; (b) UV-vis absorption spectra of the reagents used in the $\text{Co-MOF-NaIO}_4\text{-H}_2\text{O}_2$ CL system; (c) CL kinetic curves of the $\text{Co-MOF-H}_2\text{O}_2$ and the Co-MOF-NaIO_4 systems.

$(^1\text{O}_2)_2^*$ derived from reactive oxygen species (ROS) ($^1\text{O}_2$, $\cdot\text{O}_2^-$ and $\cdot\text{OH}$) was proved to be one of the luminophor molecules in the $\text{Co-MOF-NaIO}_4\text{-H}_2\text{O}_2$ system via the CL spectra (Figure 6a). Different radical scavengers and EPR spectra were used to detect the three kinds of ROS in the CL system and explore the roles that ROS played in the CL reaction process. The generation of ROS was verified by detecting the changes in the CL intensity of the $\text{Co-MOF-NaIO}_4\text{-H}_2\text{O}_2$ system before and after the addition of the specific radical scavengers. AA is an effective reactive oxygen radical quencher [42]. The CL intensity gradually decreased with increasing concentration of AA (Figure 7a). Therefore, it could be concluded that reactive oxygen radicals were produced via the $\text{Co-MOF-NaIO}_4\text{-H}_2\text{O}_2$ system and played crucial roles in the CL process. H_2O_2 could be oxidized using IO_4^- and yield $\cdot\text{O}_2^-$ [35,43]. As a free radical scavenger of $\cdot\text{O}_2^-$, BQ significantly quenched the CL intensity of the $\text{Co-MOF-NaIO}_4\text{-H}_2\text{O}_2$ system, indicating the presence of and important role played by $\cdot\text{O}_2^-$ in the CL system (Figure 7b). Thiourea and isopropanol are common $\cdot\text{OH}$ radical scavengers and were used to detect $\cdot\text{OH}$ via this CL reaction system. The addition of different concentrations of thiourea into the system was found to have an inhibitory effect on the CL intensity (Figure 7c). The same phenomenon was observed when isopropanol was added into the CL system. In total, 10 μL of isopropanol quenched more than 95% of the CL in the $\text{Co-MOF-NaIO}_4\text{-H}_2\text{O}_2$ system (Figure 7d). The reason for this outcome was that isopropanol quickly captured $\cdot\text{OH}$ to generate acetone carbonyl radicals, which then produced acetone [44]. Since isopropanol preferentially reacted with $\cdot\text{OH}$, the chances of $\cdot\text{OH}$ participating in the CL reactions were reduced, resulting in the decreased CL intensity.

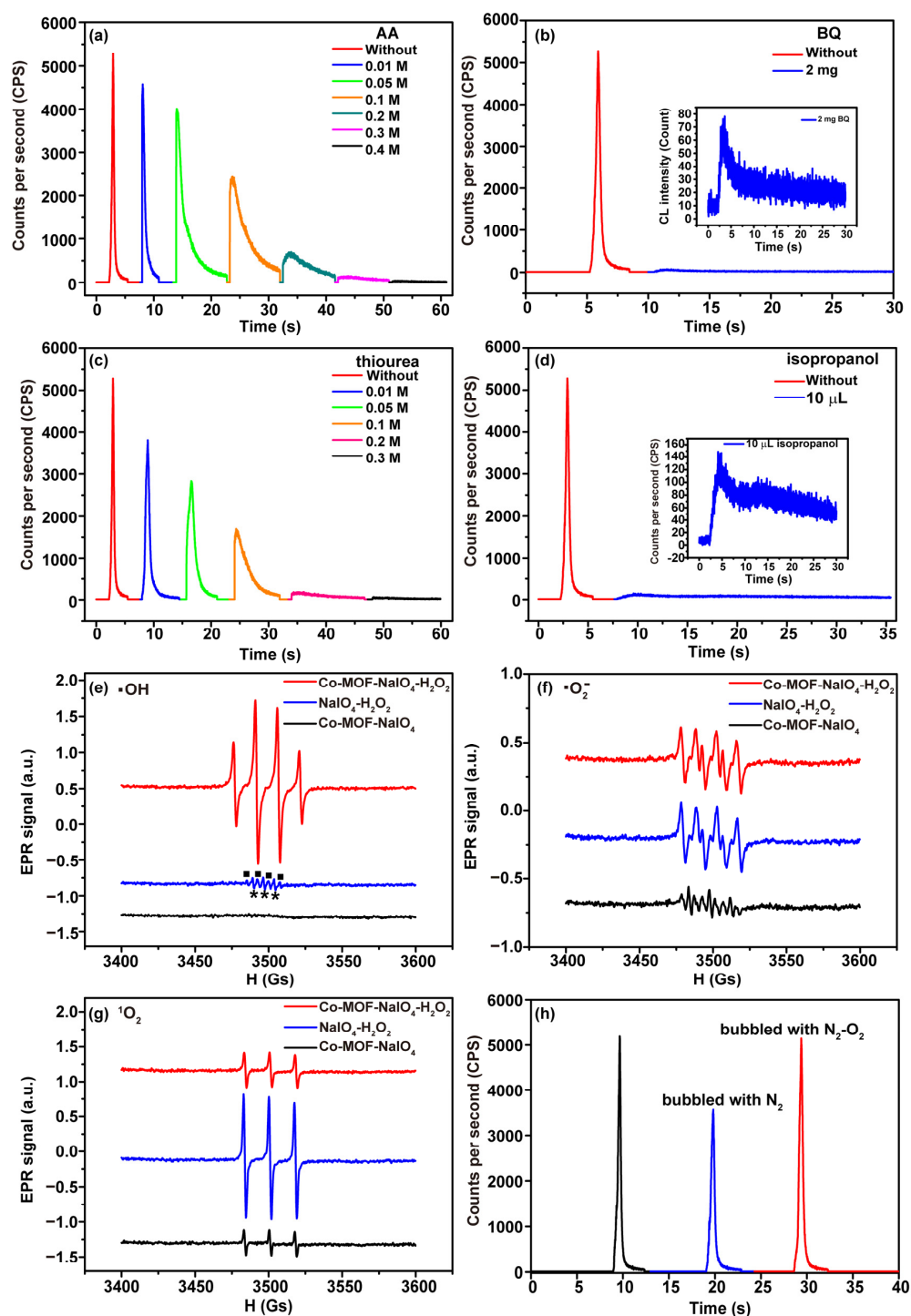


Figure 7. ROS detection in Co-MOF-NaIO₄-H₂O₂ system. (a) ROS radicals in Co-MOF-NaIO₄-H₂O₂ system were detected via AA; (b) ·O₂⁻ in Co-MOF-NaIO₄-H₂O₂ system was detected via BQ; (c) ·OH in Co-MOF-NaIO₄-H₂O₂ system was detected via thiourea; (d) ·OH in Co-MOF-NaIO₄-H₂O₂ system was detected via isopropanol; (e) ·OH was detected via EPR spectra of Co-MOF-NaIO₄-H₂O₂ system, with DMPO used as the specific scavenger agent (square symbols indicated the EPR signals of DMPO-·OH; asterisk symbols indicated the EPR signals of DMPOX); (f) ·O₂⁻ was detected via EPR spectra of Co-MOF-NaIO₄-H₂O₂ system, with DMPO used as the specific scavenger agent and CH₃OH used as the solvent; (g) ¹O₂ was detected via EPR spectra of Co-MOF-NaIO₄-H₂O₂ system, with TEMP used as the specific scavenger agent; (h) effects of dissolved oxygen on CL intensity were detected via the Co-MOF-NaIO₄-H₂O₂ system.

EPR is the most direct method used to identify radical intermediates in chemical reactions [45]. DMPO was used as the scavenger agent for $\cdot\text{OH}$ detection in the Co-MOF- $\text{NaIO}_4\text{-H}_2\text{O}_2$, $\text{NaIO}_4\text{-H}_2\text{O}_2$, and Co-MOF- NaIO_4 systems. $\cdot\text{OH}$ reacts with DMPO to form radical adduct DMPO- $\cdot\text{OH}$, which can generate a quadruple peak of EPR signals with an intensity ratio of 1:2:2:1 [46]. The characteristic EPR signals of DMPO- $\cdot\text{OH}$ were collected via the Co-MOF- $\text{NaIO}_4\text{-H}_2\text{O}_2$ system (Figure 7e, red line), which confirmed the formation of $\cdot\text{OH}$. In the absence of Co-MOF, the characteristic EPR signals of DMPO- $\cdot\text{OH}$ were also collected via the $\text{NaIO}_4\text{-H}_2\text{O}_2$ system (Figure 7e, blue line, square symbols). EPR signals of DMPO- $\cdot\text{OH}$ collected via the $\text{NaIO}_4\text{-H}_2\text{O}_2$ system decreased sharply compared to those signals collected via the Co-MOF- $\text{NaIO}_4\text{-H}_2\text{O}_2$ system, suggesting that the addition of Co-MOF promoted the decomposition of H_2O_2 to produce $\cdot\text{OH}$. There was no obvious EPR signals of DMPO- $\cdot\text{OH}$ in the Co-MOF- NaIO_4 system (Figure 7e, black line), verifying that $\cdot\text{OH}$ was derived from the decomposition of H_2O_2 . The triplet EPR signals with the intensity ratio of 1:1:1 in Figure 7e (blue line, asterisk symbols) were assigned to 5,5-dimethyl-2-oxopyrroline-1-oxyl (DMPOX), which was derived from the oxidation reaction between $^1\text{O}_2$ and DMPO [47]. DMPO is also the specific detection reagent for $\cdot\text{O}_2^-$ when CH_3OH is used as the solvent. The characteristic 1:1:1:1 quartette EPR signals of DMPO- $\cdot\text{O}_2^-$ in Figure 7f confirmed the presence of $\cdot\text{O}_2^-$ via the Co-MOF- $\text{NaIO}_4\text{-H}_2\text{O}_2$, $\text{NaIO}_4\text{-H}_2\text{O}_2$, and Co-MOF- NaIO_4 systems. IO_4^- reacted with H_2O_2 , generating $\cdot\text{O}_2^-$ and Co-MOF that accelerated this process [45]. Moreover, $\cdot\text{OH}$ derived from H_2O_2 consumed $\cdot\text{O}_2^-$ and then promoted the production of $\cdot\text{O}_2^-$. This process was the reason that the EPR signals collected via the Co-MOF- $\text{NaIO}_4\text{-H}_2\text{O}_2$ and $\text{NaIO}_4\text{-H}_2\text{O}_2$ systems were stronger than those of Co-MOF- NaIO_4 system. TEMP is a specific scavenger for $^1\text{O}_2$ and reacts with $^1\text{O}_2$ to generate TEMPO, which is a stable nitrogen oxide radical with a characteristic EPR spectrum [48]. In Figure 7g, the characteristic triplet peaks of $^1\text{O}_2$ with an intensity ratio of 1:1:1 were observed via the Co-MOF- $\text{NaIO}_4\text{-H}_2\text{O}_2$, $\text{NaIO}_4\text{-H}_2\text{O}_2$, and Co-MOF- NaIO_4 systems. $^1\text{O}_2$ was the product of the reaction between $\cdot\text{O}_2^-$ and $\cdot\text{OH}$. EPR signals collected via the $^1\text{O}_2$ in Co-MOF- $\text{NaIO}_4\text{-H}_2\text{O}_2$ system (red line) were significantly weaker than those collected via the $\text{NaIO}_4\text{-H}_2\text{O}_2$ system (blue line) because Co-MOF reacted with $(^1\text{O}_2)_2^*$, which was derived from $^1\text{O}_2$. In order to confirm whether dissolved oxygen participated in the CL process of the Co-MOF- $\text{NaIO}_4\text{-H}_2\text{O}_2$ system, nitrogen and oxygen were alternately infused into the system. The CL intensity collected via the system was significantly reduced when nitrogen was infused for 15 min (Figure 7h, blue line). The CL intensity was restored when the system was subsequently infused with O_2 for 15 min (Figure 7h, red line). It could be concluded that dissolved oxygen played an essential role in the system and reacted with IO_4^- to generate $\cdot\text{O}_2^-$ and $\cdot\text{OH}$ [43]. This reaction process explained why EPR signals of $^1\text{O}_2$ were also observed via the Co-MOF- NaIO_4 system, even though there was no H_2O_2 .

Based on the above results, the possible CL mechanism of the Co-MOF- $\text{NaIO}_4\text{-H}_2\text{O}_2$ system was inferred and shown in Figure 8. The specific reactions were described in Equations (1)–(11). Firstly, Co-MOF acted as a catalyst to decompose NaIO_4 and H_2O_2 to produce radical intermediates ($\cdot\text{OH}$ and $\cdot\text{O}_2^-$) (Equations (1) and (2)) [40,49,50]. The catalytic behavior of Co-MOF was beneficial for radical intermediate generation. IO_4^- could be oxidized using dissolved O_2 to create $\cdot\text{OH}$ and $\cdot\text{O}_2^-$ (Equation (3)) [43]. The unstable $\cdot\text{O}_2^-$ could trigger a reaction to produce $^1\text{O}_2$ (Equation (4)) [51]. $(^1\text{O}_2)_2^*$ with higher energy was generated using $^1\text{O}_2$ (Equation (5)) [40] and worked as one of the critical luminophores in the Co-MOF- $\text{NaIO}_4\text{-H}_2\text{O}_2$ system. Oxidative radicals $\cdot\text{OH}$ and IO_4^- acted as electron acceptors for Co-MOF and injected holes into Co-MOF (Equations (6) and (7)). The reductive $\cdot\text{O}_2^-$ acted as an electron donor to inject electrons into the Co-MOF (Equation (8)) [52]. Due to the CRET effect, the excited state $(^1\text{O}_2)_2^*$ transferred its energy to Co-MOF to generate Co-MOF* (Equation (9)) [53] to produce a strong CL response. The EHA effect between hole-injected Co-MOF and electron-injected Co-MOF jointly promoted

the enhanced CL collected via the Co-MOF-NaIO₄-H₂O₂ system (Equations (10) and (11)). The CRET and EHA effects together caused the strong CL release.

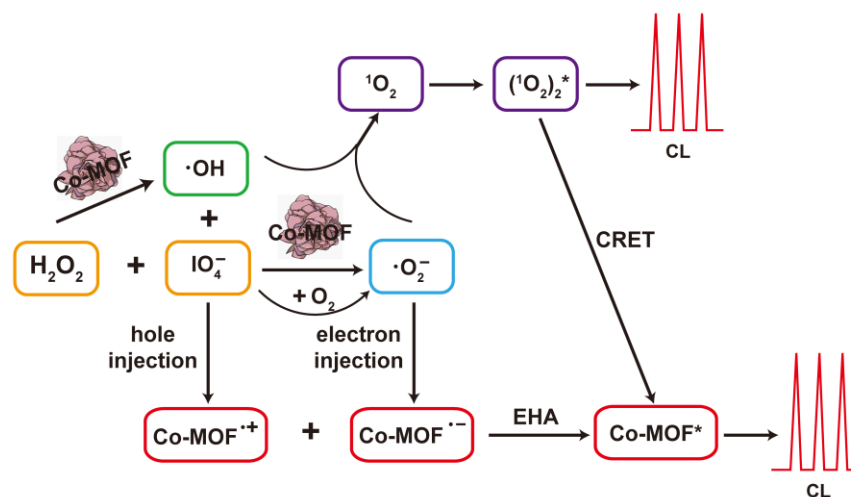
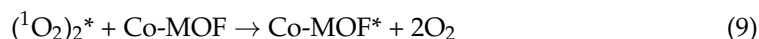
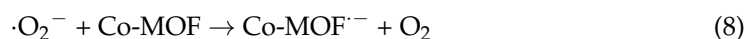
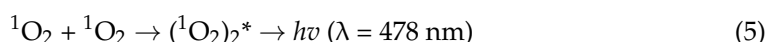
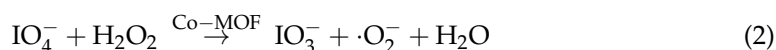


Figure 8. Schematic of the CL mechanism in the Co-MOF-NaIO₄-H₂O₂ system.

3.4. PG Detection

The Co-MOF-NaIO₄-H₂O₂ CL system constructed in this experiment was successfully used to detect PG because it could enhance the CL response. PG can be oxidized using $\cdot \text{O}_2^-$ to generate o-quinone and hydroquinone, which slowly react to yield quinone condensation products and Diels–Alder dimers [54]. These complex oxidation reactions involve forming multiple products from quinone intermediates through different reaction pathways controlled via kinetics. The oxidation process of PG is shown in Figure 9a. During this oxidation process, the excited state of singly linear oxygen (${}^1\text{O}_2^*$) was formed, and it enhanced the CL through intramolecular energy transfer. As shown in Figure 9b, the CL intensity showed a linear relationship with PG concentration in the range of 1×10^{-4} M to 1×10^{-7} M, having a linear correlation coefficient of 0.9995 and a limit of detection

(LOD) ($S/N = 3$) of 34 nM. Compared to the existing CL methods used for PG detection, the detection method described in this article has a wider linear range and lower LOD. For example, Zhuang et al. [55] developed a KIO_4 -isothiocyanatoisoluminol CL system to investigate the concentration of PG within the linear range of 1.75×10^{-8} – 2.5×10^{-6} M. Shah et al. [40] synthesized N-CDs to enhance the CL of KIO_4 - H_2O_2 systems within the linear range of 1.0×10^{-4} – 1.0×10^{-7} M and LOD of 46 nM. Mostafa et al. [10] constructed a lucigenin-PG system to detect PG, and the results showed that the LOD was 940 nM, which was higher than that of our method. Therefore, the CL detection method that we developed has a promising future in the application of PG detection.

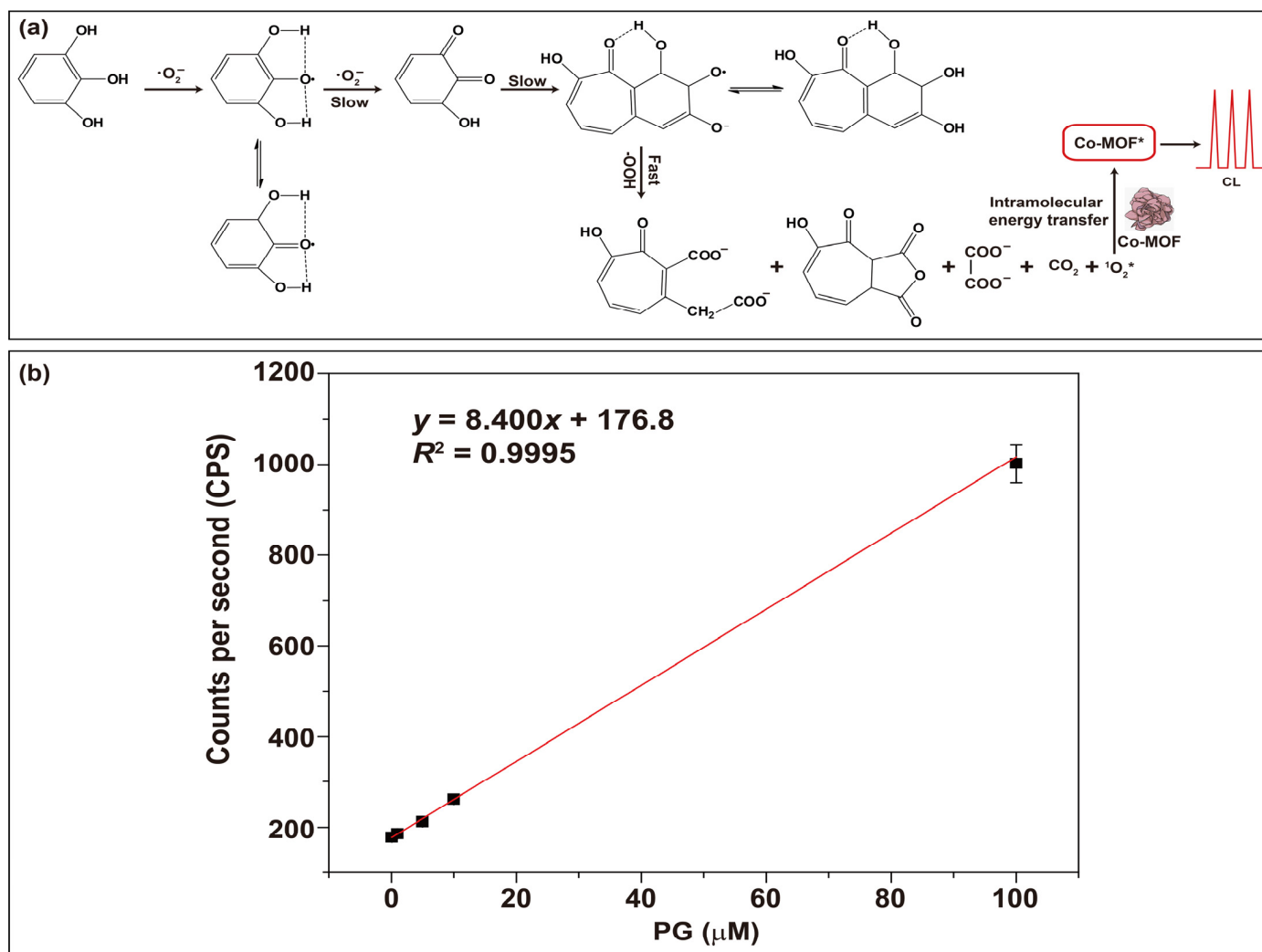


Figure 9. PG detection: (a) schematic diagram of the mechanism of PG detection; (b) standard curve used for PG detection based on the Co-MOF- $NaIO_4$ - H_2O_2 system that had a PMT operating at 1200 V.

4. Conclusions

In conclusion, the Co-MOF prepared via the ultrasonic method in this work effectively enhanced the CL signal of the $NaIO_4$ - H_2O_2 system. The Co-MOF-mediated CL enhancement was attributed to the synergistic effects of CRET and EHA. A novel CL analysis method was established for PG detection based on the quantitative relationship between the PG concentrations and the CL signal of the Co-MOF- $NaIO_4$ - H_2O_2 system. The research content and application fields of MOF materials were enriched through this work. In future work, CL analysis methods based on MOF nanomaterials are expected

to be used in multiple fields, such as clinical diagnosis, food safety, and environmental pollution monitoring.

Author Contributions: Conceptualization, Y.W.; data curation, Y.L., Z.L. and Z.G.; formal analysis, Z.W. and D.Z.; funding acquisition, J.W.; investigation, Y.W.; methodology, Y.W. and Z.W.; project administration, J.W.; resources, J.W.; supervision, J.W.; validation, K.L.; writing—original draft, Y.W.; writing—review and editing, J.W. and X.L. All authors have read and agreed to the published version of the manuscript.

Funding: This work was supported by the Beijing Natural Science Foundation (No. 2222022) and the National Natural Science Foundation of China (No. 21874120).

Data Availability Statement: The research data are available when they are requested.

Conflicts of Interest: The authors declare that they have no known competing financial interests or personal relationships that could have appeared to influence the work reported in this paper.

References

1. Li, Z.; Yang, Y.; Zeng, Y.; Wang, J.; Liu, H.; Guo, L.; Li, L. Novel imidazole fluorescent poly(ionic liquid) nanoparticles for selective and sensitive determination of pyrogallol. *Talanta* **2017**, *174*, 198–205. [[CrossRef](#)] [[PubMed](#)]
2. Shin, M.; Park, E.; Lee, H. Plant-inspired pyrogallol-containing functional materials. *Adv. Funct. Mater.* **2019**, *29*, 1903022. [[CrossRef](#)]
3. Singh, V.; Ahmad, S.; Rao, G.S. Prooxidant and antioxidant properties of iron-hydroquinone and iron-1,2,4-benzenetriol complex—implications for benzene toxicity. *Toxicology* **1994**, *89*, 25–33. [[CrossRef](#)] [[PubMed](#)]
4. Gao, Y.N.; Fu, Q.Q.; Lu, J.; Yang, H.; Orr, P.T.; Zhang, F.; Dong, J.; Zhang, M.; Gu, Q.H.; Zhou, C.J.; et al. Enhanced pyrogallol toxicity to cyanobacterium *Microcystis aeruginosa* with increasing alkalinity. *J. Appl. Phycol.* **2020**, *32*, 1827–1835. [[CrossRef](#)]
5. Hamed, M.; Martyniuk, C.J.; Said, R.E.M.; Soliman, H.A.M.; Badrey, A.E.A.; Hassan, E.A.; Abdelhamid, H.N.; Osman, A.G.M.; Sayed, A.E.H. Exposure to pyrogallol impacts the hemato-biochemical endpoints in catfish (*Clarias gariepinus*). *Environ. Pollut.* **2023**, *333*, 122074. [[CrossRef](#)]
6. He, S.; He, D.; Jiang, H. Fi-chemiluminescence determination of pyrogallol in water. *Phys. Test. Chem. Anal.* **2008**, *44*, 316–318.
7. Park, W.H.; Han, Y.H.; Kim, S.H.; Kim, S.Z. Pyrogallol, ROS generator inhibits As4.1 juxtaglomerular cells via cell cycle arrest of G2 phase and apoptosis. *Toxicology* **2007**, *235*, 130–139. [[CrossRef](#)]
8. Rajkumar, C.; Kim, H. An amperometric electrochemical sensor based on hierarchical dual-microporous structure polypyrrole nanoparticles for determination of pyrogallol in the aquatic environmental samples. *Microchem. J.* **2022**, *183*, 108038. [[CrossRef](#)]
9. Torrini, F.; Renai, L.; Scarano, S.; Del Bubba, M.; Palladino, P.; Minunni, M. Colorimetric selective quantification of anthocyanins with catechol/pyrogallol moiety in edible plants upon zinc complexation. *Talanta* **2022**, *240*, 123156. [[CrossRef](#)]
10. Mostafa, I.M.; Gilani, M.; Chen, Y.Q.; Lou, B.H.; Li, J.P.; Xu, G.B. Lucigenin-pyrogallol chemiluminescence for the multiple detection of pyrogallol, cobalt ion, and tyrosinase. *J. Food Drug Anal.* **2021**, *29*, 510–520. [[CrossRef](#)]
11. Bao, A.; Xiao, N.; Zhu, Y.C.; Xin, S.G.; Zhang, H.B. The electrochemical catalytic behavior of pyrogallol at an 8-hydroxyquinoline-aluminum complex modified carbon paste electrode and its detection in tomato. *RSC Adv.* **2015**, *5*, 12710–12716. [[CrossRef](#)]
12. Matemadombo, F.; Apetrei, C.; Nyokong, T.; Rodriguez-Mendez, M.L.; de Saja, J.A. Comparison of carbon screen-printed and disk electrodes in the detection of antioxidants using copc derivatives. *Sensor. Actuat. B-Chem.* **2012**, *166*, 457–466. [[CrossRef](#)]
13. Chen, F.; Xia, X.; Ye, D.; Li, T.; Huang, X.; Cai, C.; Zhu, C.; Lin, C.; Deng, T.; Liu, F. A green-emitting luminol analogue as the next-generation chemiluminescent substrate in biochemical analysis. *Anal. Chem.* **2023**, *95*, 5773–5779. [[CrossRef](#)]
14. Yuan, S.J.; Yu, R.; Tu, Y.; Du, Y.H.; Feng, X.; Nie, F. An enhanced chemiluminescence hybrids of luminol by sulfonated polyaniline decorated copper-based metal organic frame composite applicable to the measurement of hydrogen peroxide in a wide pH range. *Talanta* **2023**, *254*, 124183. [[CrossRef](#)]
15. Li, J.L.; Yang, M.Q.; Cao, D.; Zhang, L.; Zong, C.; Li, P. Ultrasensitive homogeneous detection of pcsk9 and efficacy monitoring of the pcsk9 inhibitor based on proximity hybridization-dependent chemiluminescence imaging immunoassay. *Anal. Chem.* **2023**, *95*, 5428–5435. [[CrossRef](#)]
16. Sun, M.X.; Song, H.J.; Liu, H.Y.; Su, Y.Y.; Xie, X.B.; Lv, Y. Organic semiconductor nanosheets for sulfite detecting based on activation of sulfite and a synergetic chemiluminescence resonance energy transfer process in a mild system of Fe^{2+} - SO_3^{2-} . *Anal. Chem.* **2023**, *95*, 3901–3908. [[CrossRef](#)]
17. Chang, J.F.; Yu, L.; Hou, T.; Hu, R.X.; Li, F. Direct and specific detection of glyphosate using a phosphatase-like nanozyme-mediated chemiluminescence strategy. *Anal. Chem.* **2023**, *95*, 4479–4485. [[CrossRef](#)]
18. Yang, M.; Huang, J.; Fan, J.; Du, J.; Pu, K.; Peng, X. Chemiluminescence for bioimaging and therapeutics: Recent advances and challenges. *Chem. Soc. Rev.* **2020**, *49*, 6800–6815. [[CrossRef](#)]
19. Yan, Y.; Wang, X.; Hai, X.; Song, W.; Ding, C.; Cao, J.; Bi, S. Chemiluminescence resonance energy transfer: From mechanisms to analytical applications. *Trac-Trend. Anal. Chem.* **2020**, *123*, 115755. [[CrossRef](#)]

20. Zhu, H.; Huang, X.; Deng, Y.; Chen, H.; Fan, M.; Gong, Z. Applications of nanomaterial-based chemiluminescence sensors in environmental analysis. *Trac-Trend. Anal. Chem.* **2023**, *158*, 116879. [[CrossRef](#)]
21. Zong, C.; Wu, J.; Zang, Y.; Ju, H.X. Resonance energy transfer and electron-hole annihilation induced chemiluminescence of quantum dots for amplified immunoassay. *Chem. Commun.* **2018**, *54*, 11861–11864. [[CrossRef](#)] [[PubMed](#)]
22. Ma, X.; Kang, J.; Wu, Y.; Pang, C.; Li, S.; Li, J.; Xiong, Y.; Luo, J.; Wang, M.; Xu, Z. Recent advances in metal/covalent organic framework-based materials for photoelectrochemical sensing applications. *Trac-Trend. Anal. Chem.* **2022**, *157*, 116793. [[CrossRef](#)]
23. Ren, X.; Liao, G.; Li, Z.; Qiao, H.; Zhang, Y.; Yu, X.; Wang, B.; Tan, H.; Shi, L.; Qi, X.; et al. Two-dimensional MOF and COF nanosheets for next-generation optoelectronic applications. *Coordin. Chem. Rev.* **2021**, *435*, 213781. [[CrossRef](#)]
24. Singh, M.; Kumar, G.; Neogi, S. Devising mixed-ligand based robust Cd(II)-framework from bi-functional ligand for fast responsive luminescent detection of Fe³⁺ and Cr(VI) oxo-anions in water with high selectivity and recyclability. *Front. Chem.* **2021**, *9*, 651866. [[CrossRef](#)]
25. Liu, B.; Hou, L.; Wu, W.P.; Dou, A.N.; Wang, Y.Y. Highly selective luminescence sensing for Cu²⁺ ions and selective CO₂ capture in a doubly interpenetrated MOF with lewis basic pyridyl sites. *Dalton Trans.* **2015**, *44*, 4423–4427. [[CrossRef](#)] [[PubMed](#)]
26. Rühle, B.; Virmani, E.; Engelke, H.; Hinterholzinger, F.M.; von Zons, T.; Brosent, B.; Bein, T.; Godt, A.; Wuttke, S. A chemiluminescent metal-organic framework. *Chem-Eur. J.* **2019**, *25*, 6349–6354. [[CrossRef](#)]
27. Vaitsis, C.; Sourkouni, G.; Argiris, C. Metal organic frameworks (MOFs) and ultrasound: A review. *Ultrason. Sonochem.* **2019**, *52*, 106–119. [[CrossRef](#)]
28. Zhao, S.; Wang, Y.; Dong, J.; He, C.; Yin, H.; An, P.; Zhao, K.; Zhang, X.; Gao, C.; Zhang, L.; et al. Ultrathin metal-organic framework nanosheets for electrocatalytic oxygen evolution. *Nat. Energy* **2016**, *1*, 16184. [[CrossRef](#)]
29. Zhang, L.; Ouyang, H.; Zhang, D.; Fu, Z. Novel cobalt-based metal-organic frameworks with superior catalytic performance on n-(4-aminobutyl)-n-ethylisoluminol chemiluminescent reaction. *Anal. Chim. Acta* **2021**, *1148*, 238174. [[CrossRef](#)]
30. Wang, S.; Zhao, Y.; Wang, M.; Li, H.; Saqib, M.; Ge, C.; Zhang, X.; Jin, Y. Enhancing luminol electrochemiluminescence by combined use of cobalt-based metal organic frameworks and silver nanoparticles and its application in ultrasensitive detection of cardiac troponin i. *Anal. Chem.* **2019**, *91*, 3048–3054. [[CrossRef](#)]
31. Zhong, H.; Ly, K.H.; Wang, M.; Krupskaya, Y.; Han, X.; Zhang, J.; Zhang, J.; Kataev, V.; Büchner, B.; Weidinger, I.M.; et al. A phthalocyanine-based layered two-dimensional conjugated metal-organic framework as a highly efficient electrocatalyst for the oxygen reduction reaction. *Angew. Chem. Int. Edit.* **2019**, *58*, 10677–10682. [[CrossRef](#)]
32. Tirosh, E.; Shemer, G.; Markovich, G. Optimizing cobalt ferrite nanocrystal synthesis using a magneto-optical probe. *Chem. Mater.* **2006**, *18*, 465–470. [[CrossRef](#)]
33. Shyamaldas; Bououdina, M.; Manoharan, C. Dependence of structure/morphology on electrical/magnetic properties of hydrothermally synthesised cobalt ferrite nanoparticles. *J. Magn. Magn. Mater.* **2020**, *493*, 165703. [[CrossRef](#)]
34. Yang, J.; Xiong, P.; Zheng, C.; Qiu, H.; Wei, M. Metal-organic frameworks: A new promising class of materials for a high performance supercapacitor electrode. *J. Mater. Chem. A* **2014**, *2*, 16640–16644. [[CrossRef](#)]
35. Huang, C.; Wang, Y.; Wang, Y.; Chen, T.; Wu, J.; Liu, X.; Lin, C. Ultraweak chemiluminescence enhanced on the surface of lanthanide metal-organic framework nanosheets synthesized by ultrasonic wave. *Appl. Surf. Sci.* **2022**, *579*, 151860. [[CrossRef](#)]
36. Wang, Y.F.; Wang, Y.R.; Huang, C.X.; Chen, T.Y.; Wu, J. Ultra-weak chemiluminescence enhanced by cerium-doped LaF₃ nanoparticles: A potential nitrite analysis method. *Front. Chem.* **2020**, *8*, 639. [[CrossRef](#)]
37. Wang, Y.; Huang, C.; Wang, Y.; Chen, T.; Wu, J. Chemiluminescence enhanced by cerium-doped LaF₃ nanoparticles through electron-hole annihilation. *J. Lumin.* **2021**, *239*, 118407. [[CrossRef](#)]
38. Shah, S.N.A.; Khan, M.; Rehman, Z.U. A prolegomena of periodate and peroxide chemiluminescence. *Trac-Trend. Anal. Chem.* **2020**, *122*, 115722. [[CrossRef](#)]
39. Adam, W.; Kazakov, D.V.; Kazakov, V.P. Singlet-oxygen chemiluminescence in peroxide reactions. *Chem. Rev.* **2005**, *105*, 3371–3387. [[CrossRef](#)]
40. Shah, S.N.A.; Li, H.; Lin, J. Enhancement of periodate-hydrogen peroxide chemiluminescence by nitrogen doped carbon dots and its application for the determination of pyrogallol and gallic acid. *Talanta* **2016**, *153*, 23–30. [[CrossRef](#)]
41. Cai, N.; Yang, D.Q.; He, Y.Y.; Chen, F.N. Enhanced chemiluminescence of the fluorescein-KIO₄ system by cdte quantum dots for determination of catechol. *Luminescence* **2018**, *33*, 871–876. [[CrossRef](#)] [[PubMed](#)]
42. Li, R.; Kameda, T.; Toriba, A.; Hayakawa, K.; Lin, J. Determination of benzo[a]pyrene-7,10-quinone in airborne particulates by using a chemiluminescence reaction of hydrogen peroxide and hydrosulfite. *Anal. Chem.* **2012**, *84*, 3215–3221. [[CrossRef](#)] [[PubMed](#)]
43. Zheng, Y.Z.; Zhang, D.K.; Shah, S.; Li, H.F.; Lin, J.M. Ultra-weak chemiluminescence enhanced by facilely synthesized nitrogen-rich quantum dots through chemiluminescence resonance energy transfer and electron hole injection. *Chem. Commun.* **2017**, *53*, 5657–5660. [[CrossRef](#)] [[PubMed](#)]
44. Lai, D.Z.; Lu, W.Y.; Liu, T.; Fu, Y.Q.; Yi, L.M.; Chen, W.X. Peroxy radical formation from Cu₂O/poly(acrylonitrile) nanofibers and hydrogen peroxide. *Sci. Adv. Mater.* **2016**, *8*, 775–782. [[CrossRef](#)]
45. Sun, X.; Lei, J.; Jin, Y.; Li, B. Long-lasting and intense chemiluminescence of luminol triggered by oxidized g-C₃N₄ nanosheets. *Anal. Chem.* **2020**, *92*, 11860–11868. [[CrossRef](#)]
46. Liu, H.J.; Sun, M.X.; Su, Y.Y.; Deng, D.Y.; Hu, J.Y.; Lv, Y. Chemiluminescence of black phosphorus quantum dots induced by hypochlorite and peroxide. *Chem. Commun.* **2018**, *54*, 7987–7990. [[CrossRef](#)]

47. Zhang, W.Y.; Fernandez-Fueyo, E.; Ni, Y.; van Schie, M.; Gacs, J.; Renirie, R.; Wever, R.; Mutti, F.G.; Rother, D.; Alcalde, M.; et al. Selective aerobic oxidation reactions using a combination of photocatalytic water oxidation and enzymatic oxyfunctionalizations. *Nat. Catal.* **2018**, *1*, 55–62. [[CrossRef](#)]
48. Chance, B.; Sies, H.; Boveris, A. Hydroperoxide metabolism in mammalian organs. *Physiol. Rev.* **1979**, *59*, 527–605. [[CrossRef](#)]
49. Xie, C.G.; Li, H.F. Determination of tannic acid in industrial wastewater based on chemiluminescence system of $\text{KIO}_4\text{-H}_2\text{O}_2\text{-tween40}$. *Luminescence* **2010**, *25*, 350–354. [[CrossRef](#)]
50. Huang, T.Y.; Lin, W.Y. A stopped-flow study of the dual chemiluminescence for the luminol- $\text{KIO}_4\text{-Mn}^{2+}$ system in strong alkaline solutions. *Luminescence* **2011**, *26*, 118–124. [[CrossRef](#)]
51. Lin, Z.; Xue, W.; Chen, H.; Lin, J. Peroxynitrous-acid-induced chemiluminescence of fluorescent carbon dots for nitrite sensing. *Anal. Chem.* **2011**, *83*, 8245–8251. [[CrossRef](#)]
52. Shah, S.; Zheng, Y.Z.; Li, H.F.; Lin, J.M. Chemiluminescence character of ZnS quantum dots with bisulphite-hydrogen peroxide system in acidic medium. *J. Phys. Chem. C* **2016**, *120*, 9308–9316. [[CrossRef](#)]
53. Dou, X.N.; Lin, Z.; Chen, H.; Zheng, Y.Z.; Lu, C.; Lin, J.M. Production of superoxide anion radicals as evidence for carbon nanodots acting as electron donors by the chemiluminescence method. *Chem. Commun.* **2013**, *49*, 5871–5873. [[CrossRef](#)]
54. Evmiridis, N.P.; Vlessidis, A.G.; Thanasoulas, N.C.; Fritsky, I.O. Chemical analysis through Cl^- -detection assisted by periodate oxidation. *Bioinorg. Chem. Appl.* **2007**, *2007*, 92595. [[CrossRef](#)]
55. Zhuang, H.S.; Wang, Q.E.; Wu, F. Study on the chemiluminescence (CL) analysis for the determination of pyrogallol in water environment. *Spectrosc. Spect. Anal.* **2004**, *24*, 927–929.

Disclaimer/Publisher's Note: The statements, opinions and data contained in all publications are solely those of the individual author(s) and contributor(s) and not of MDPI and/or the editor(s). MDPI and/or the editor(s) disclaim responsibility for any injury to people or property resulting from any ideas, methods, instructions or products referred to in the content.